J Appl Electrochem (2007) 37:1413–1427
DOI 10.1007/s10800-007-9353-x

ORIGINAL PAPER

Activity, selectivity, and methanol tolerance of novel carbon-supported Pt and Pt_3Me (Me = Ni, Co) cathode catalysts

L. Colmenares · E. Guerrini · Z. Jusys · K. S. Nagabhushana · E. Dinjus · S. Behrens · W. Habicht · H. Bönnemann · R. J. Behm

Received: 21 December 2006 / Revised: 24 April 2007 / Accepted: 29 April 2007 / Published online: 18 July 2007

Abstract The activity, selectivity, and methanol tolerance of novel, carbon supported high-metal loading (40 wt.%) Pt/C and Pt_3Me/C (Me = Ni, Co) catalysts for the O_2 reduction reaction (ORR) were evaluated in model studies under defined mass transport and diffusion conditions, by rotating (ring) disk and by differential electrochemical mass spectrometry. The catalysts were synthesized by the organometallic route, via deposition of pre-formed Pt and Pt_3Me pre-cursors followed by their decomposition into metal nanoparticles. Characteristic properties such as particle sizes, particle composition and phase formation, and active surface area, were determined by transmission electron microscopy, energy dispersive X-ray spectroscopy, X-ray photoelectron spectroscopy, and X-ray diffraction. For comparison, commercial Pt/C catalysts (20 and 40 wt.%, E-Tek, Somerset, NJ, USA) were investigated as well, allowing to evaluate Pt loading effects and, by comparison with the pre-cursor-based catalyst with their much smaller particle sizes (1.7 nm diameter), also particle size effects. Kinetic parameters for the ORR were evaluated; the ORR activities of the bimetallic catalysts and of the synthesized Pt/C catalyst were comparable and similar to that of the high-loading commercial Pt/C catalyst; at typical cathode operation potentials H_2O_2 formation is negligible for the synthesized catalysts. Due to their lower methanol oxidation activity the bimetallic catalysts show an improved methanol tolerance compared to the commercial Pt/C catalysts. The results indicate that the use of very small particle sizes is a possible way to achieve reasonably good ORR activities at an improved methanol tolerance at DMFC cathode relevant conditions.

Keywords Oxygen reduction · Bimetallic catalyst · Methanol tolerance · Activity · Selectivity · DEMS · R(R)DE

L. Colmenares · E. Guerrini · Z. Jusys · R. J. Behm (✉)
Institute of Surface Chemistry and Catalysis, Ulm University, 89069 Ulm, Germany
e-mail: juergen.behm@uni-ulm.de

Present Address:
E. Guerrini
Department of Physical Chemistry and Electrochemistry, University of Milan, Milan 20133, Italy

K. S. Nagabhushana · E. Dinjus · S. Behrens · W. Habicht · H. Bönnemann
Forschungszentrum Karlsruhe, ITC-CPV, Postfach 3640, 76021 Karlsruhe, Germany

K. S. Nagabhushana · E. Dinjus
Karls-Rupprecht-Universität, Heidelberg, Seminarstrasse 2, 69117 Heidelberg, Germany

1 Introduction

The overpotential for the oxygen reduction reaction (ORR) at low-temperature polymer electrolyte fuel cell (PEFC) cathodes is one of the major factors limiting the PEFC performance. Furthermore, in the Direct Methanol Fuel Cell (DMFC), the cross-over of methanol from the anode to the cathode side results in parasitic methanol oxidation on the cathode at typical operation potentials, which leads to the formation of a 'mixed potential' [1–3] and additional performance losses, especially, on Pt cathode catalysts. Therefore, the development of cathode catalysts with improved ORR performance and methanol tolerance is one of the major challenges in low-temperature fuel cell electrocatalysis.

The state-of-the-art cathode catalysts for low-temperature fuel cells are mostly bimetallic Pt-based nanoparticles

supported on a conductive high-surface area carbon support. Several PtMe alloys (Me = Co [4, 5], Ni [4–6], Fe [4, 7], and Cr [8, 9], etc.) have been investigated in rotating (ring) disk electrode (R(R)DE) model studies and were shown to be promising candidates for low-temperature fuel cell cathode catalyst, demonstrating both improved ORR performance and methanol tolerance.

In recent years, a number of 'methanol tolerant' cathode catalysts have been reported, such as Ru selenide-based catalysts [10–13] or metal containing macrocycles (porphyrins, phenantrolins) [14–18], which would be attractive also due to the reduced costs, since they are not based on noble metals. General problem of these catalysts, however, are their too low-activity compared to standard Pt/C cathode catalysts or even state-of-the-art bimetallic PtMe/C catalyst [19], and their greater tendency for H_2O_2 formation at fuel cell relevant cathode operating potentials [12, 13, 19].

A different approach would be to optimize Pt/C or PtMe/C noble metal catalysts with respect to a higher methanol tolerance. This would avoid the significant activity losses connected with the above catalysts, although the cost situation would be improved only by the extent of the increasing ORR activity. One possible route for doing this would be to move to smaller particle sizes. Small Pt particles have been demonstrated to be more oxophillic, i.e., more easily oxidizable [20], and on the other side it is well known that on oxidized/OH_{ad} covered Pt surfaces/particles methanol oxidation is inhibited, at least at potentials <1 V_{RHE}, leaving very small Pt particles less active for the methanol oxidation reaction (MOR) [21, 22]. The particle size effects in the MOR have to be compared with particle size effects in the ORR. It has been reported that the active surface area normalized ORR activity increases with the particle size until a maximum is reached at about 3.5 nm, based on comparative studies on series of different Pt catalysts [8, 23, 24]. On the other hand, Watanabe et al. found no particle size effect for the ORR, and assumed that this effect is dependent on the intercrystallite distance and not on the dimensions of the Pt crystallites [25], and similar conclusions of a Pt particle size independent ORR activity were also reported by Yano et al. [26].

This strategy is also the topic of the present paper where we report results of a comprehensive electrocatalytic model study on the activity, selectivity (H_2O_2 formation) and methanol tolerance of novel, carbon supported Pt/C and non-alloyed, bimetallic Pt_3Me/C (Me = Co, Ni) catalysts in the ORR. For comparison, we included two commercial Pt/C catalysts with different Pt loading (E-Tek Inc., 20 and 40 wt.% Pt), which also allowed conclusions on possible noble metal loading effects. The catalysts were synthesized via the so-called organometallic route, depositing preformed colloidal Pt, and Pt_3Me pre-cursors on a high-surface area carbon support (see below) [27–30]. In contrast to the commonly applied method for preparing carbon-supported PtMe alloy catalysts, involving deposition of the non-precious metal on a carbon-supported Pt catalyst prepared beforehand, followed by alloying at high temperatures ($T > 700$ °C), we expect this method to avoid substantial metal particle growth by sintering and coalescence during the high-temperature treatment. The resulting catalysts were characterized with respect to particle sizes and particle size distribution, chemical composition, and phase formation by transmission electron microscopy (TEM), energy dispersive X-ray spectroscopy (EDX), photoelectron spectroscopy (XPS), and X-ray diffraction (XRD). The electrochemical and electrocatalytic properties of the catalysts were determined by potentiodynamic rotating ring disk electrode (RRDE) and differential electrochemical mass spectrometry (DEMS) measurements under controlled electrolyte flow and partly at elevated temperatures (RRDE). This involved (1) the determination of the active surface area by pre-adsorbed CO monolayer oxidation, via CO_2 detection in the DEMS set-up, (2) the determination of the ORR kinetic current densities (Tafel plots) normalized to the metal mass, the geometric surface area, or the active surface area, (3) the selectivity in the ORR (O_2 reduction to H_2O_2) as measured by RRDE measurements, (4) the activity and selectivity (complete oxidation of methanol to CO_2) in the MOR as evaluated from DEMS measurements, and (5) the mutual interaction between MOR and ORR at elevated temperatures as measured by RDE in methanol free and methanol containing, O_2-saturated electrolyte.

2 Experimental

2.1 Commercial (E-Tek) catalysts

Commercial Pt/C catalysts (E-Tek) of different loading (Pt loading 20 and 40 wt.%) were used as a reference. The mean particle sizes were *ca.* 3.7 nm [31] and 3.0 nm [32] for the Pt/C with 20 and 40 wt.%, respectively. This also allowed to evaluate the effect of the Pt/C catalyst loading on the ORR and MOR activity/selectivity.

2.2 Synthesis of 40 wt.% Pt/C, Pt_3Co/C, and Pt_3Ni/C catalysts

$Pt(CH_3)_2COD$ (COD = 1,5 cyclooctadiene) was obtained from $Pt(acac)_2$ (acac = acetylacetonate) (Strem Chemicals, Newburyport, MA, USA) by reacting with trimethylaluminum in a single step reaction to yield the product in more than 90%. This synthetic procedure was described in details recently [30]. The synthesis was performed under strict argon conditions. The solvents used for the reaction

were thoroughly dried. Starting materials and the low-valent complexes were used after necessary purifications.

For the Pt/C catalyst, $Pt(CH_3)_2COD$ was added to a dispersion of Black Pearl in toluene (Fluka, Milwaukee, WI, USA, >99.5% purity), being stirred under a constant flow of argon. After stirring the suspension for 1 h at room temperature, the solvent was evaporated under reduced pressures and the raw catalyst was conditioned under a flow of H_2 at 150 °C for 2 h. The temperature was limited to 150 °C to remove the organic impurities and to prevent any agglomeration or sintering. This way, it was attempted to synthesize catalysts, which are sufficiently stable under fuel cell conditions on the one hand and which, on the other hand, retain the advantage of the low-temperature preparation, yielding very small particles sizes.

For the Pt_3Ni/C and Pt_3Co/C catalysts, the crystallized $Pt(CH_3)_2COD$ was dissolved in toluene, to which $Co_2(CO)_8$ or $Ni(COD)_2$ (Strem Chemicals) were added to obtain Pt and Co(Ni) in an atomic ratio of 3:1. To this solution, Black Pearl carbon support was added to obtain 40 wt.% total metal on carbon. Conditioning was performed by reduction in a H_2 flow at an initial temperature of 120 °C for Pt_3Co and 50 °C for Pt_3Ni (owing to the volatility of the $Ni(COD)_2$), after 2 min the temperature was ramped to 250 °C in H_2 (4 °C min^{-1}), and kept there for 1.5 h. Higher conditioning temperatures were avoided to keep particle sintering or agglomeration at low levels.

For transmission electron microscopic (TEM) measurements, the catalysts were first dissolved in an alcohol solution and sonicated (3 min), then they were placed on a carbon-coated Cu grid. Electron microscopy data were then collected using a Philips Tecnai F20 TEM with a field emission gun operated at 200 kV. Scanning electron microscopy (SEM) imaging was performed on a LEO Gemini 982 SEM equipped with a LINK ISIS 300 EDX analysis unit from Oxford Corp. X-ray diffractograms were measured using a Siemens D5000 instrument, operating with Cu $K\alpha$ radiation (λ = 0.15406 nm). Scans were recorded at 0.12 min^{-1} for 2θ values from 20 to 100°. XP spectra were obtained on a Physical Electronics instrument (System 5800) using monochromatized Al-$K\alpha$ radiation.

2.3 Thin-film electrode preparation

The thin-film electrodes were prepared as described previously [31], by pipetting 20 µl aliquot of an aqueous suspension (2 mg ml^{-1}) of the catalyst onto the glassy carbon disk (Sigradur G, from Hochtemperatur Werkstoffe, Thierhaupten, Germany), and after drying the catalyst was fixed with a defined amount (20 µl) of diluted aqueous Nafion solution on top of the dried catalyst layer. The latter results in a very thin (*ca.* 0.1 µm thickness) Nafion film, which is thin enough to avoid additional diffusion resistance, but thick enough to ensure a sufficient physical stability of the catalyst layer [31, 33]. The geometric area of the accessible part of the electrode is 0.283 cm^2, the metal loading is 28 (20 wt.% Pt loading), and 56 µg cm^{-2} (40 wt.% Pt loading). In earlier work, we had shown that agglomeration and utilization effects are negligible in this loading regime [34]. The same experimental procedure was applied for preparation of working electrodes for R(R)DE and DEMS measurements. Before the electrochemical measurements, the catalysts were cleaned by cycling in base electrolyte until a constant CV was obtained (initial potential 0.06 V, upper potential: 1.36 V for Pt/C for about ten cycles and then 1.16 V, and 0.5 V for Pt_3Me/C catalysts, in order to avoid leaching of Ni or Co).

2.4 RRDE measurements

The RRDE measurements for the ORR (in the absence and presence of methanol) were performed in a thermostated three-compartment electrochemical cell at 60 °C and 1,600 rpm. A Pt wire and a saturated calomel electrode (SCE) were used as counter and reference electrode, respectively. The working electrode was installed into a commercial (Pine Instruments, Grove City, PA, USA) ring-disk head with an exchangeable disk (6 mm in diameter) surrounded by an insulating Teflon U-cup and embedded Pt ring. Ring and disk potentials were controlled separately by a bi-potentiostat (Pine Instruments). The ring collection efficiency, N, was confirmed to be *ca.* 20% [33] at a rotation rate of 1,600 rpm and a ring potential of 1.2 V versus the reversible hydrogen electrode (RHE). Hydrogen peroxide yields, $x(H_2O_2)$, were calculated from the ring (I_R) and disk (I_D) currents via the equation: $x(H_2O_2) = (2I_R/N)/(I_D + I_R/N)$. The mass transport-normalized kinetic ORR currents at the disk electrode were calculated as $I_k = I_{lim} \times I/(I_{lim} - I)$ and are given as mass, geometric or active surface (determined by CO_{ad} stripping) area specific kinetic ORR currents in the Tafel plots.

2.5 DEMS measurements

The DEMS set-up consisted of two differentially pumped chambers, a Balzers QMS 112 quadrupole mass spectrometer, a Pine Instruments potentiostat, and a computerized data acquisition system. DEMS measurements were performed in a dual thin-layer flow-through DEMS cell [35, 36] at an electrolyte flow of *ca.* 10 µl s^{-1}, with the working electrode in the first compartment and a porous membrane positioned in the second compartment. Two Pt wires at the inlet and outlet of the flow-cell, and a SCE connected to the outlet through a Teflon capillary served as counter and reference electrode, respectively.

The active surface area of the Pt/C (commercial catalyst) was derived from the charge for hydrogen underpotential adsorption (H_{upd}) at potentials between 0.06 and 0.36 V, subtracting a double-layer charging contribution, and from the CO_2 signal obtained during oxidation of a saturated CO adlayer ('CO_{ad} stripping'), following the procedure described in [36]. From the H_{upd} adsorption charge in the base CV the active (Pt) surface area was estimated, assuming that the H_{upd} coverage at the onset of bulk hydrogen evolution is 0.77 [37] and that the hydrogen monolayer adsorption charge on polycrystalline Pt is equal to 0.21 mC cm^{-2} [38].

CO_{ad} stripping was performed following the procedure described in [36]. Briefly, CO was pre-adsorbed at a constant electrode potential (0.06 V) for 10 min, by injecting 2 ml of CO-saturated 0.5 M H_2SO_4 solution through a separate port. After CO adsorption, the cell was carefully flushed with Ar-saturated supporting electrolyte (0.5 M H_2SO_4 solution) at the same electrode potential. The CO adlayer was stripped at a potential scan rate of 10 mV s^{-1}, starting from the adsorption potential and recording both Faradaic and m/z = 44 ion current. The second potential cycle of the CO-free electrode was also recorded for comparison. From the mass spectrometric charge for CO_2 production during CO_{ad} stripping, the active surface area of the novel Pt/C, and binary catalysts was calculated, for the Pt/C catalyst (commercial) the CO_2 formation charge was calibrated against the H-upd charge.

The current efficiencies for the complete oxidation of methanol to CO_2 on the different catalysts were calculated following the procedure described elsewhere [34, 36]. From the potentiostatic measurement (potential-step from 0.06 to 0.6 V, and then stepwise to 0.7 and 0.8 V; 300 s per potential to reach steady-state conditions) the current efficiencies were determined from the partial mass spectrometric current for CO_2 formation relative to the total MOR Faradaic current using the calibration constant (K^*) determined for oxidation of a saturated CO adlayer (CO_{ad} stripping) (see [34, 36]).

The supporting electrolyte (0.5 M sulfuric acid) was prepared using Millipore Q water, ultrapure sulfuric acid (Merck, Hohenbrumn, Germany, suprapur), and 10 mM methanol in supporting electrolyte was prepared using methanol from Merck (p.a.). The electrolyte was deaerated by high-purity Ar (MTI Gase, N 6.0) or saturated with O_2 (MTI Gase, N 5.7). For the CO stripping experiments the electrolyte was saturated with CO (Messer-Griesheim, N 4.7). All potentials are quoted versus that of the RHE.

3 Results and discussion

3.1 Physical characterization

The TEM images recorded on the different synthesized catalysts show a uniform distribution of the metal nanoparticles with no pronounced agglomeration of the particles for all catalysts (Fig. 1). The Pt nanoparticles had a very low-particle size and a narrow size distribution (1.7 ± 0.4 nm) (Fig. 1a). For a 40 wt.% metal loading catalyst this particle size is remarkably small, considering that there was no stabilizer used for the preparation, in contrast to the standard colloidal preparation route [39]. The very small Pt particle sizes are presumably favored by the very high-surface area of the Black Pearl carbon support (~1,400 m^2 g^{-1}). It should be noted that using $Pt(a\text{-}cac)_2$ directly as a starting material for the catalyst synthesis results in very non-homogeneous particle distributions, containing large particles as well, unsuitable for catalytic purposes. TEM images of the catalysts also reveal very small particles with sizes down to 0.8 nm. Similarly, the Pt_3Co particles were also relatively small with the average particle size in the range of 2.0 ± 0.3 nm (Fig. 1b). The particle size is rather close to that of the pure Pt nanoparticles. Spontaneous decomposition of both cobalt and platinum complexes enables a burst of nucleation at the initial temperature of 120 °C, followed by controlled growth (during the temperature ramp) to result in monodisperse nanoparticles under the H_2 environment. Most importantly, it is the non-volatile nature of the cobalt complex that helps in the formation of bimetallic catalysts with a homogeneous distribution of the components. For the Pt_3Ni/C catalyst, the situation is much different. $Ni(COD)_2$ has a melting (decomposition) temperature of 60 °C and is volatile, therefore, the initial temperature of conditioning was 50 °C. This also means that $Ni(COD)_2$ melts and decomposes much earlier than the Pt complex during the temperature ramp, resulting in larger particle sizes. This is indeed observed in the TEM measurements (Fig. 1c), the average particle size for Pt_3Ni/C catalyst is 3.6 ± 0.9 nm.

The EDX analysis of Pt_3Me/C catalysts confirmed the metal ratio in the expected nominal compositions (see Table 1), and comparable ratios were also obtained from XPS for Pt_3Co/C, while for Pt_3Ni/C the Ni(2p) intensity was lower than expected from the metal ratio, which would be compatible with the formation of larger Ni particles (see discussion below). XRD scans of the carbon supported Pt/C and bimetallic Pt_3Me/C catalysts show the five characteristic peaks of the face-centered cubic (fcc) crystalline Pt, corresponding to the (111), (200), (220), (311), and (222) planes (Fig. 2). The Co containing catalysts shows significant peak broadening due to the small particle size. The other two samples exhibit sharp profiles with a broadened base, which could point to a mixture of smaller and larger particles. The lattice parameters of the Pt_3Me/C catalysts (Me = Ni, Co) catalysts are within <0.0005 nm identical to those of the Pt/C catalysts (Table 1, column 4), indicating that the bimetallic Pt_3Co/C and Pt_3Ni/C catalyst particles

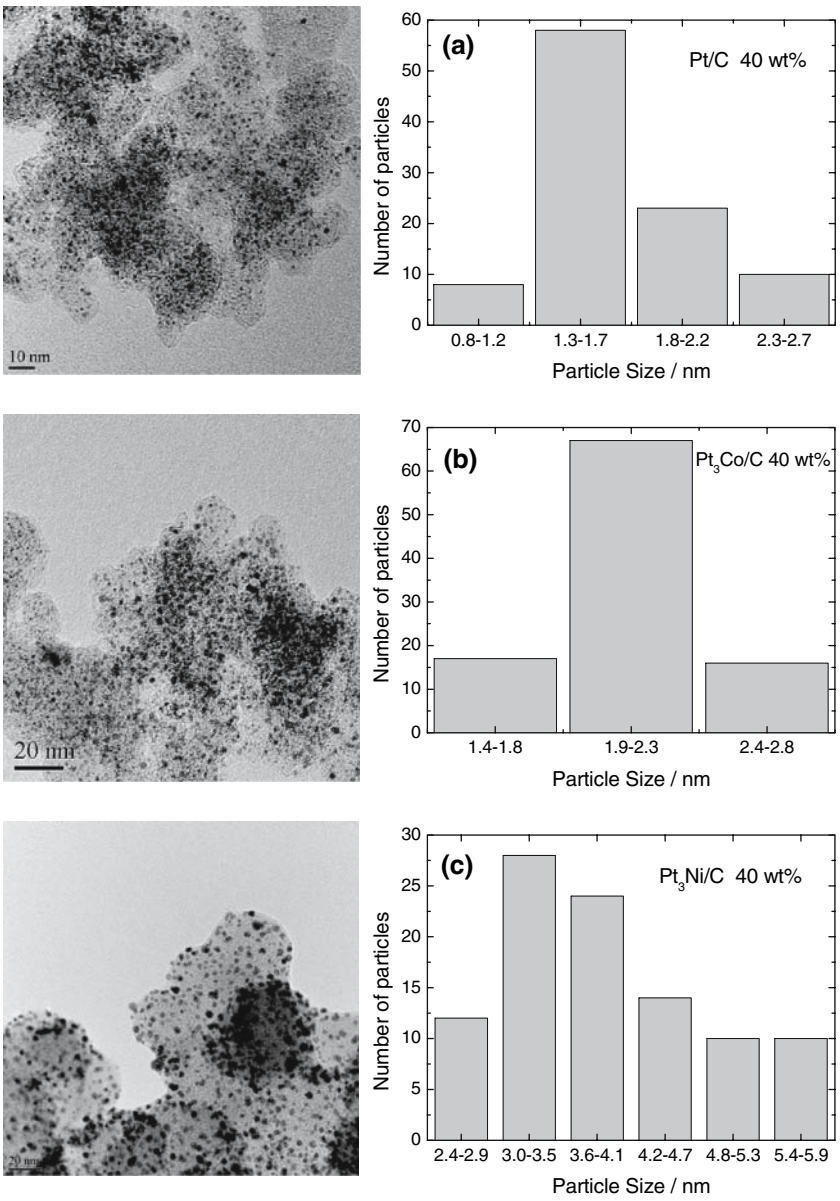

Fig. 1 TEM and the corresponding histogram indicating the particle size distribution of **a** Pt/C; **b** Pt_3Co/C and **c** Pt_3Ni/C 40 wt.% catalysts

Table 1 EDX, TEM, XRD, and active surface area calculated from mean particle size, CO_{ad} stripping and H_{upd} of carbon supported Pt/C (commercial and synthesized) and bimetallic Pt_3Me/C (Me = Ni, Co) catalysts

Catalysts	EDX	TEM	XRD	Surface area (cm^2)		
	Pt : Me (a/o)	Mean particle size (nm)	Lattice parameter (Å)	Theoretical	CO_{ad} stripping	H_{upd}
Pt/C (20 wt.% E-Tek)	–	3.7 ± 1[a]	–	6.1	–	6.4
Pt/C (40 wt.% E-Tek)	–	3.0[b]	–	14.9	12.6	12.3
Pt/C (40 wt.%)	–	1.7 ± 0.4	3.914	25.2	22.3	20.1
Pt_3Co/C (40 wt.%)	2.4:1	2.0 ± 0.2	3.914	25.0	22.9	–
Pt_3Ni/C (40 wt.%)	2.9:1	3.6 ± 0.9	3.910	14.6	23.0	–

[a] After conditioning [31]

[b] Ref. [32]

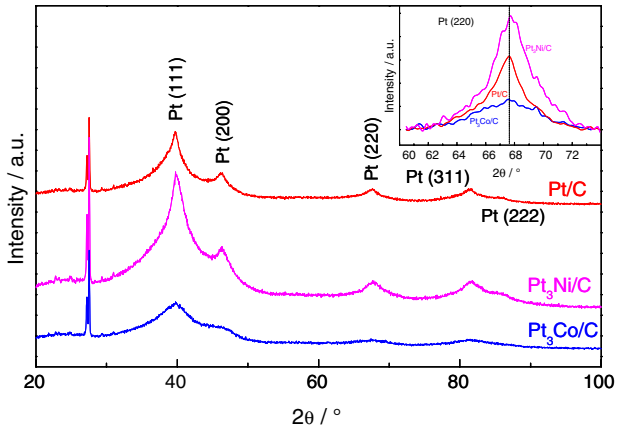

Fig. 2 XRD patterns of the synthesized 40 wt.% Pt/C and 40 wt.% Pt_3Me/C (Me = Co and Ni) catalysts. The *inset* shows the enlarged Pt(220) diffraction peaks

consisted of a mixture of almost pure Pt and pure, amorphous Ni(Co) phases, or their respective oxides, while alloy formation could essentially be ruled out. No metallic Co or Ni signals were observed.

3.2 Active surface area determination

The active surface area for all catalysts used in this report was calculated from the ratio of the CO_2 signal during oxidation of a saturated CO adlayer ('CO_{ad} stripping') to that on Pt/C (E-Tek, 20 wt.%) catalyst. The calculated surface areas (from the mean particle size and CO_{ad} stripping) of the commercial Pt/C catalysts (E-Tek Inc., 20 and 40 wt.% Pt loading) and of the synthesized carbon-supported Pt and Pt_3Me(Me = Ni, Co) 40 wt.% catalysts are collected in Table 1.

3.2.1 Commercial Pt/C catalysts

Faradaic current as well as mass spectrometric CO_{ad} stripping traces (first positive-going scan) as well as a base voltammogram recorded on these catalysts are shown in Fig. 3a and b. The CO_{ad} stripping features and the subsequent base CVs fully (Fig. 3a) resemble those reported previously for Pt/C (E-Tek) catalyst [36, 40], with a complete suppression of H_{upd} features at the CO_{ad} blocked Pt surface in the H_{upd} potential range (0.06–0.35 V), the onset of CO_{ad} oxidation at potentials positive of 0.35 V, in the so-called pre-wave, and the distinct CO_{ad} oxidation peak centered at 0.8 V. The onset of the CO_{ad} oxidation in the pre-wave region is shown in a magnified representation in the inset of Fig. 3b. Obviously, the pre-wave is more pronounced on the higher loading catalyst. At potentials positive of 0.9 V, oxygen adsorption sets in. In the subsequent scan we find PtO reduction at 0.8 V in the negative-going scan and hydrogen adsorption/desorption features between 0.06 and 0.35 V. As expected, the current increases significantly with the Pt loading (28 μg cm^{-2} for Pt/C 20 wt.% and 56 μg cm^{-2} for Pt/C 40 wt.%) [34], reflecting the about double Pt surface area for the higher loading catalyst due to the rather similar particle size (see Table 1).

The corresponding active surface areas of the Pt/C (E-Tek) catalysts (Table 1) can be compared with the theoretical surface area, which was calculated from the mean particle diameter assuming spherical particles [41]. For both catalysts, in particular for the 20 wt.% catalyst, these values agree well, implying complete surface utilization for these catalysts. The slightly lower experimental value of the Pt surface area of the 40 wt.% catalyst may be related to some particle agglomeration at this high loading. If the particle size for the 40 wt.% Pt/C (E-Tek) is calculated from the active surface area, we obtain a value of *ca.* 3.5 ± 0.1 nm.

3.2.2 Synthesized catalysts

Similar CO_{ad} stripping experiments were performed on the synthesized catalysts (Fig. 3c, d). For the Pt/C catalyst, the H-upd charge was evaluated as described above, for the bimetallic catalyst the surface area was determined by CO_{ad} stripping (mass spectrometric CO_2 detection) to avoid artifacts caused by oxidation/dissolution of the non-noble metal in the Faradaic current. The active (Pt) surface areas calculated this way are listed in Table 1.

The CO_{ad} stripping curve and the base voltammogram recorded on the synthesized Pt/C (40 wt.%) catalysts resemble the ones obtained on the 40 wt.% Pt/C (E-Tek, Fig. 3a) catalyst in their general characteristics, but differ in some quantitative aspects. Despite the similar Pt loading of both catalysts, the latter catalyst exhibits about doubled H_{upd}, PtO formation/reduction, and CO_{ad} stripping features (Fig. 3c, d), which is explained by the distinct difference in the mean particle size (*ca.* 1.7 nm) compared to that for commercial 40 wt.% Pt/C (*ca.* 3.0 nm), which results in a pronounced increase in the catalyst surface area for the novel 40 wt.% Pt/C catalyst, as shown in Table 1. Apparently, the addition of Co or Ni does not improve the activity for CO_{ad} oxidation (Fig. 3c, d). Based on the mass spectrometric CO_2 signal, CO_2 formation starts at about 0.3 V, similar to Pt/C (see inset Fig. 3d). With increasing potential this pre-wave CO_{ad} oxidation increases significantly faster than on the 40 wt.% synthesized Pt/C catalyst and also faster than on the commercial 40 wt.% Pt/C catalyst. The main CO_{ad} oxidation peak is centered at 0.8 V, similar as for the synthesized Pt/C catalyst, but in total the peaks are broader than on Pt/C. In the negative-going scan, the PtO reduction peak on the Pt_3Me/C catalysts is shifted about 0.1 V negatively compared to Pt/C.

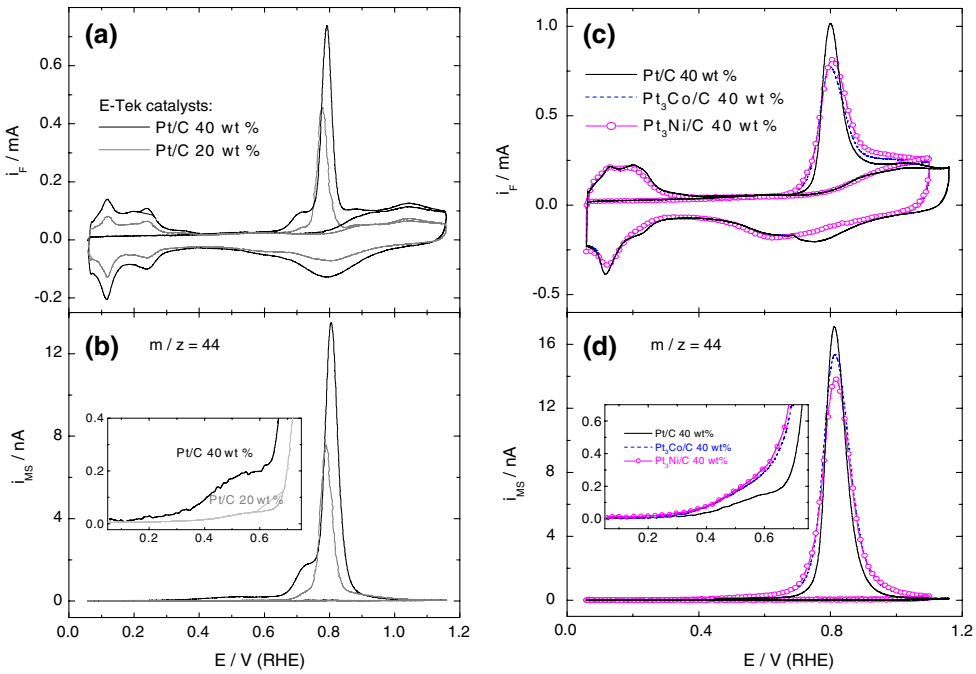

Fig. 3 Preadsorbed (E_{ad} = 0.06 V, t_{ad} ~ 10 min) CO_{ad} monolayer oxidation (stripping) on Pt/C (20 and 40 wt.%; E-Tek) and on novel Pt/C and Pt_3Me/C (Me = Ni and Co), 40 wt.% catalysts in a DEMS configuration: Faradaic (**a**, **c**) and mass spectrometric *m/z* = 44 (**b**, **d**) current dependence on the electrode potential (CVs and MSCVs, correspodingly). *Inset* Fig. 3b and d: magnified pre-wave region. Catalyst loading 28 and 56 μg cm^{-2} for 20 and 40 wt.%, respectively, electrolyte (0.5 M H_2SO_4) flow rate 10 μl s^{-1}, potential scan rate 10 mV s^{-1}, room temperature

For the Pt/C (40 wt.%) and the Pt_3Co/C (40 wt.%) catalysts the active surface areas determined by CO_{ad} stripping (22.3 and 22.9 cm^2, respectively), agrees well with the surface areas calculated from the mean particle size (25.2 and 25.0 cm^2, respectively). For the calculation of the active surface area of the Pt_3Co/C and Pt_3Ni/C catalysts we assumed an average density of Pt and Co(Ni) equal to 18.3 g cm^{-3} (75% Pt, 21.45 g cm^{-3} and 25% Co(Ni), 8.9 g cm^{-3}). The active surface area determined from CO_{ad} stripping for Pt_3Ni/C (23.0 cm^2) was similar to that determined for Pt_3Co/C, but significantly higher than the theoretical surface (14.6 cm^2) calculated from the mean particle size (3.6 nm). Calculating the particle size from the surface area determined by CO_{ad} stripping, the value obtained is *ca.* 2 nm, which is comparable to the mean particle size of pure Pt/C catalyst (1.7 nm). The discrepancy between the theoretical surface area and the active surface area for Pt_3Ni/C, together with the XRD and TEM data, points to phase separation between Pt and Ni, possibly even in separate particles with larger Ni particles. This may possibly result from the very different decomposition temperatures of the Pt and Ni pre-cursors, which may lead to a more pronounced phase separation and larger, separate Ni particles, coexistent with smaller Pt-rich particles. On Pt_3Co/C, XRD data also exclude crystalline alloy formation, but the calculated surface area fits much better to the active (Pt) surface areas, indicating that the TEM-based particle size distribution properly describes the behavior of Pt.

3.3 Oxygen reduction reaction (ORR)

To evaluate the electrocatalytic activity of the novel Pt/C and bimetallic Pt_3Me/C (Me = Ni, Co) catalysts and, for comparison, of the commercial Pt/C (20 and 40 wt.%, E-Tek) catalysts in the ORR, the selectivity for the different ORR pathways (incomplete oxygen reduction to hydrogen peroxide versus complete reduction to water), and the kinetic ORR parameters (Tafel plots), we performed a series of RRDE measurements on thin-film model electrodes of the respective catalysts in O_2-saturated 0.5 M H_2SO_4 electrolyte at 60 °C and 1,600 rpm, i.e., under fuel cell relevant conditions (realistic catalysts, continuous mass transport, elevated temperatures). The Pt catalyst loading (E-Tek, 28 and 56 μg_{Pt} cm^{-2}) and the Ni/Co related effects on the ORR activity/selectivity will be discussed in Sects. 3.3.1 and 3.3.2, respectively.

3.3.1 Pt catalyst loading effects

The RRDE results on the 20 and 40 wt.% commercial Pt/C catalysts are shown in Fig. 4a and b. As expected, the mass-transport limited ORR current on the Pt/C disk obtained at potentials negative of 0.6 V (Fig. 4a) does not depend on the catalyst loading. The well-defined diffusion limited currents for the ORR in this potential region are followed by a mixed kinetic and diffusion controlled region between 0.7 and 1.0 V, where the cathodic currents decrease toward more positive potentials. The current trace is

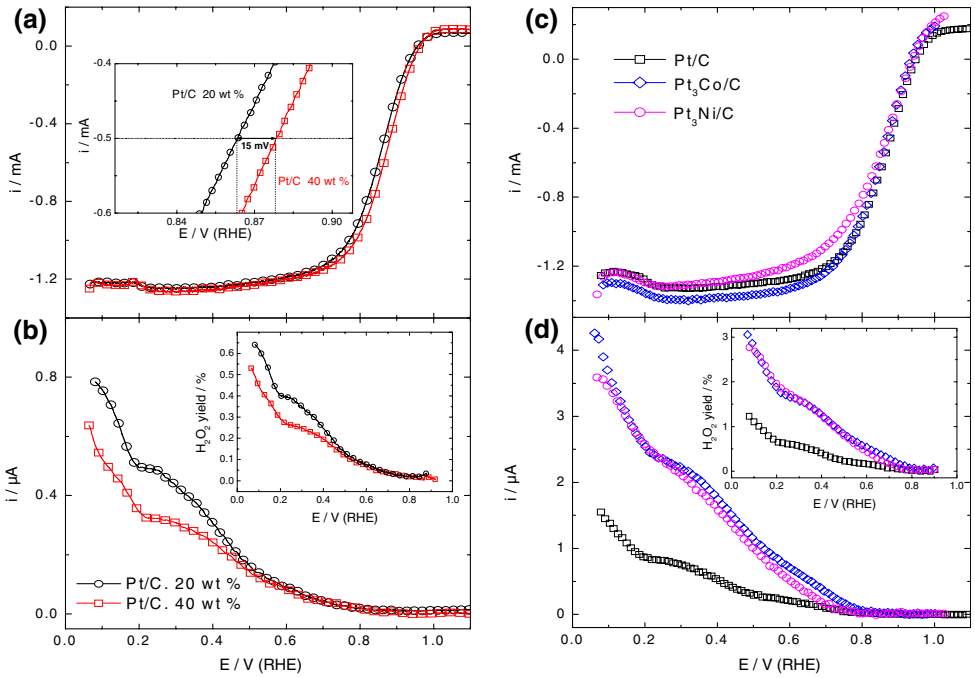

Fig. 4 O_2 reduction current (**a**, **c**), H_2O_2 formation current (**b**, **d**), and H_2O_2 yields (*inset* **b** and **d**) on Pt/C (20 and 40 wt.%; E-Tek) and on novel Pt/C and Pt_3Me/C (Me = Ni and Co) 40 wt.% catalysts measured by R(R)DE: positive-going potential scans in O_2-saturated 0.5 M H_2SO_4 electrolyte. Catalyst loading 28 and 56 μg cm^{-2} for 20 and 40 wt.%, respectively (*disk*), polycrystalline Pt ring (E = 1.2 V, collection efficiency 20%), rotation rate 1,600 rpm, potential scan rate 10 mV s^{-1}, 60 °C temperature

shifted positively by *ca.* 15 mV for the higher Pt loading (40 wt.%) catalyst (Fig. 4a, inset). Since this shift disappears upon the current normalization versus the active surface area, it simply results from the higher Pt loading (larger Pt surface area in the kinetically controlled region).

The selectivity of the ORR was evaluated by the oxidation of the hydrogen peroxide formed under the present reaction conditions on the Pt ring (biased at constant potential of 1.2 V) (Fig. 4b, d). It reaches its maximum value (yield of *ca.* 0.6%, Fig. 4b, inset) at the negative potential limit on the H_{upd} blocked catalyst (Fig. 4a). In the H_{upd} region a decreasing of the H_2O_2 yields (Fig. 4b, inset) is observed on Pt/C (40 wt.%), due to the high-Pt loading (catalyst layer thickness) and increased probability for further reduction of H_2O_2 to water. Hydrogen peroxide production is less in the double-layer potential region, where the surface is blocked by anions of supporting electrolyte (HSO_4^-), and is fully absent at potentials more positive of 0.8 V (at typical fuel cell cathode operation potentials), indicating that the ORR proceeds preferably through a $4e^-$ reduction pathway, in agreement with literature data [33, 42].

For better comparison, the normalized kinetic ORR currents obtained at 60 °C are replotted in Tafel plots (Fig. 5a–c) as function of the potential (0.7–1.0 V), showing (a) the geometric surface area normalized kinetic current, (b) the inherent catalytic activity, normalized to the active (Pt) surface area (calculated from CO_{ad} stripping), and (c) the Pt mass specific current densities in order to compare the activities on electrodes with different metal loadings (Pt/C, 20 or 40 wt.%, E-Tek).

Under present reaction conditions, the ORR activities of the commercial catalysts are nearly identical when normalized to the metal loading (mass specific) or the active surface area (inherent catalytic activity), in contrast to the measured (absolute) current or the geometric area normalized current. At 0.9 V, the 20 wt.% Pt/C catalyst exhibits a slightly higher mass specific (Fig. 5c) and inherent (Fig. 5b) ORR activity (*ca.* 1.3 times) compared to the 40 wt.% Pt/C catalyst. In contrast, the geometric surface area normalized Tafel plot (Fig. 5a), which does not account for different loadings or active surface areas, shows a higher activity (about 1.5 times) for the 40 wt.% Pt/C catalyst at the same potential. These trends differ somewhat from the results reported by Higuchi et al., who found that the active surface area-specific ORR activity at 0.76 or 0.8 V is about constant, irrespective of the Pt loading, over a wide range of Pt/C catalysts, from 19.2 to 62.3 wt.% in Pt/CB (CB: Carbon Black) at $w_{Pt} \leq 7.08$ μg_{Pt} cm^{-2} [43]. At higher Pt loading, they also find a decay of the active surface area specific activity. Effects of the Pt particle size, which are different for the two commercial Pt/C catalysts investigated here, were reported by Peuckert et al. and Kinoshita, who found an optimun Pt particle size of 3.5 nm for the ORR [23, 24].

3.3.2 *Synthesized catalysts*

The results of similar measurements on the ORR activity (Fig. 4c) and selectivity (Fig. 4d, inset) obtained on the synthesized Pt/C and bimetallic Pt_3Me/C (Me = Ni, Co) catalysts are shown in Fig. 4. The general characteristic of

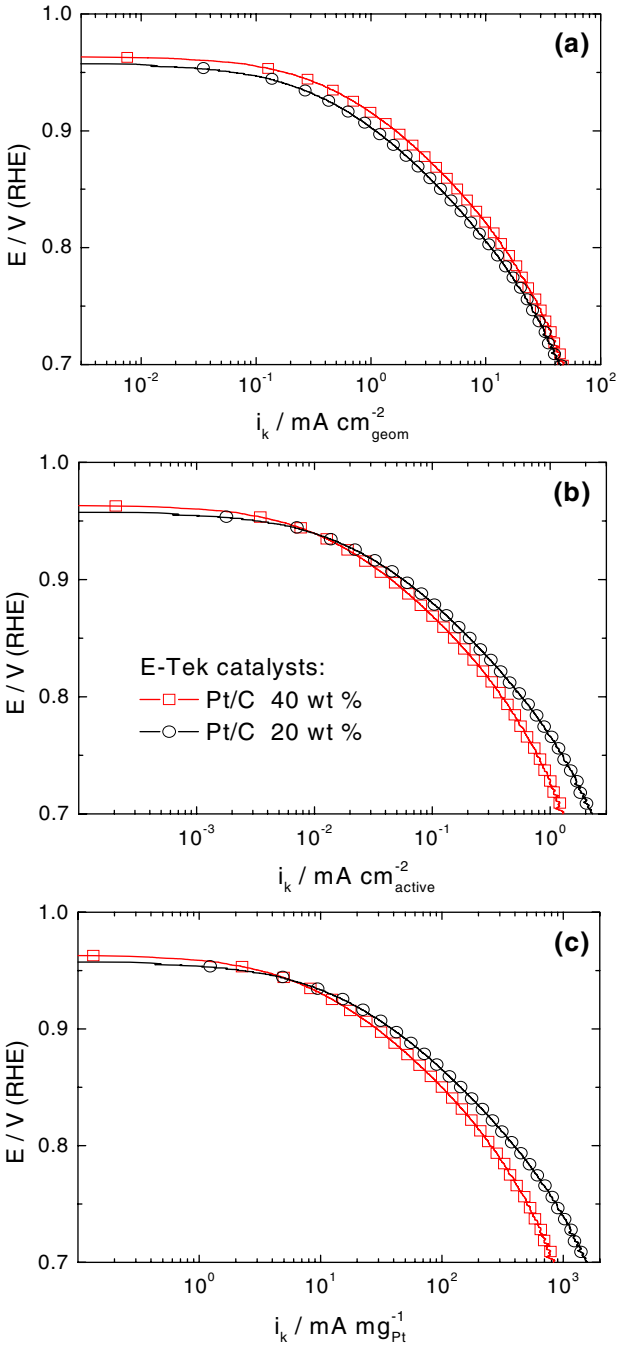

Fig. 5 Geometric area normalized (**a**), active surface area normalized (**b**), and Pt mass normalized (**c**) kinetic currents in the ORR as a function of applied potential on Pt/C (20 and 40 wt.%; E-Tek) catalyst. Data extracted from Fig. 4

the current–potential curves resemble those of the commercial Pt/C catalyst (Fig. 4a, b), with a mixed kinetic-mass transport limited region ($0.7 < E < 1.0$ V), followed by a well-defined mass transport region (0.2 V $< E < 0.7$ V). The bimetallic catalysts exhibit a comparable ORR activity (onset of O_2 reduction) as the Pt/C catalyst, resembling previously reported data for Pt alloy catalysts, alloyed with Ni or Co, of similar composition [5, 44]. This is different for massive alloy electrodes, where a significant improvement in ORR performance was reported [45].

A kinetic analysis of the ORR currents in the mixed kinetic-mass transport controlled region (0.7–0.95 V) yielded the Tafel plots in Fig. 6, reproducing the geometric area (Fig. 6a), active surface area (Fig. 6b), and mass specific (Fig. 6c) normalized kinetic reaction rates. From a mechanistic point of view, the active surface area normalized rates, normalized to the active Pt surface area determined from CO_{ad} stripping, is more relevant than the geometric area or mass normalized kinetic currents, which are commonly referred to for technical applications, because it reflects the inherent ORR activity of the active surface sites. The Tafel plots show the typical trends reported for the ORR on Pt, with a change in slope from a low-slope region at low overpotentials to a high-slope region at higher overpotentials, but still in the kinetically controlled region, with a continuous transition between the two regions [46]. Similar to the data in Fig. 4, the Tafel plots do not indicate a Co- or Ni-induced improvement of the ORR activity under the present reaction conditions (catalyst loading: 56 μg_{metal} cm^{-2}, 60 °C, 1,600 rpm, and 0.5 M H_2SO_4) compared to the synthesized Pt/C catalyst. This agrees with the absence of electronic effects for the ORR expected for non-alloyed bimetallic catalysts. Comparing with the commercial Pt/C catalyst, we find higher (inherent) active surface area normalized activity for the commercial Pt/C catalysts, but, due to the much lower particle sizes of the synthesized catalysts, the geometric area normalized values are about equal for similar Pt loading.

The hydrogen peroxide formation (ORR selectivity) on these catalysts plotted in Fig. 4d shows a slight increase on the Pt/C (40 wt.%) catalyst compared to that on the commercial E-Tek catalyst at the same loading (Fig. 4b), most likely due to the distinctly smaller particle size. Decreasing particle sizes have been reported to increase the oxophilicity of the particles and enhance the adsorption of anion due to the changes in the electronic surface properties (for a detailed discussion see [20]). On the bimetallic catalysts Pt_3Me/C (Me = Ni, Co), H_2O_2 formation is clearly higher than on the Pt/C catalyst, increasing continuously at potentials negative of 0.7 V, until a maximum value of around 3% is reached in the H_{upd} region (Fig. 4d, inset). Similar trends were also reported for carbon-supported Pt-based alloy PtNi(Co)/C catalysts [5] and on polycrystalline Pt_3Ni and Pt_3Co alloys [47] and in sputtered Pt_2Co and Pt_2Ni catalysts [48]. It should be noted, however, that in these studies alloy formation was clearly demonstrated, where the resulting dilution effects can much easier explain an increase in H_2O_2 formation. The increase of H_2O_2 formation in the H-upd range has been attributed to Pt

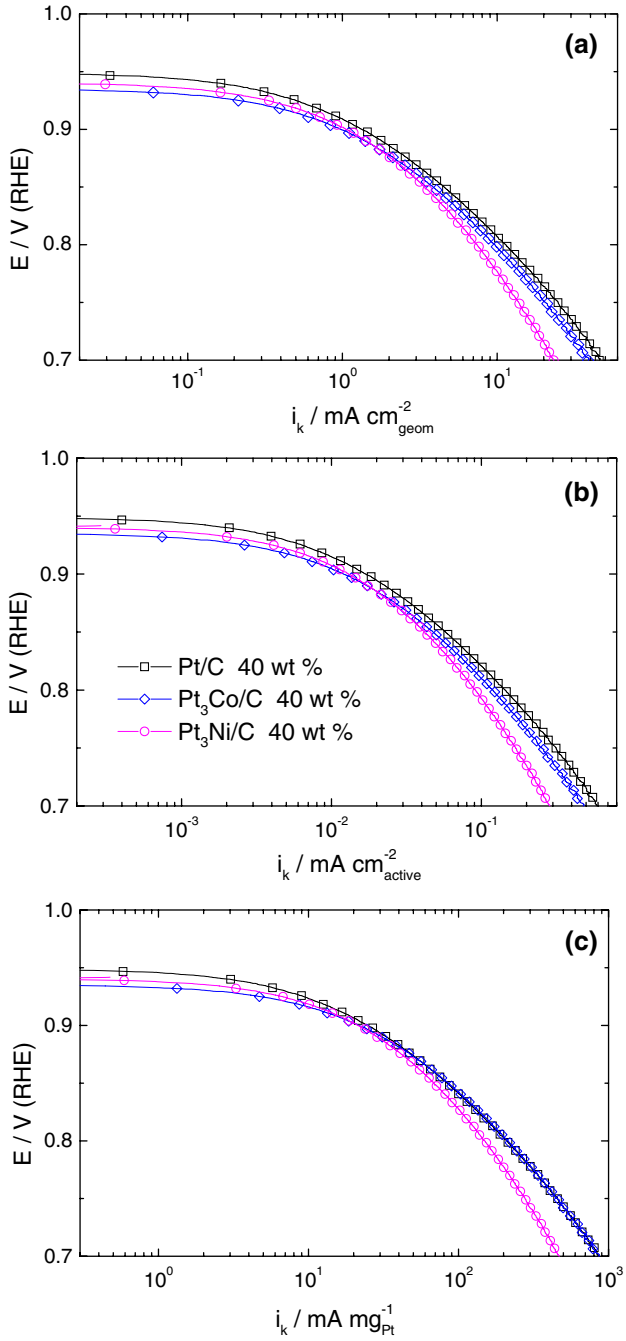

Fig. 6 Geometric area normalized (**a**), active surface area normalized (**b**), and mass normalized (**c**) kinetic currents in the ORR as a function of applied potential on the Pt/C and Pt_3Me/C (Me = Ni and Co) catalysts. Data extracted from Fig. 4

blocking by adsorbed hydrogen [49, 50]. Finally, it is important to note, that at potentials relevant for cathode operation (positive of 0.7 V) the hydrogen peroxide production on Pt_3Me/C (Me = Ni, Co) catalysts is negligible and comparable to that on the Pt/C catalyst.

In total, the ORR activity of the synthesized Pt and bimetallic Pt_3Me catalysts was close to that of the commercial Pt/C catalysts (for similar loading), when comparing geometrical area normalized or metal mass normalized values, despite of the much smaller particle sizes of the synthesized particles. Correspondingly, the active surface area normalized ORR activity, describing the inherent activity of the catalysts, was somewhat lower than that of the commercial catalysts, i.e., the advantage of the smaller particle size of the synthesized catalysts is largely compensated by their lower inherent activity. H_2O_2 formation (ORR selectivity) is slightly higher on the synthesized Pt/C catalyst than on the commercial Pt/C catalysts, and again higher on the bimetallic catalysts, amounting to 0.3, 0.1, and 1.0% at 0.5 V, respectively. At potentials relevant for cathode operation ($E > 0.7$ V), the H_2O_2 production was negligible for all catalysts (<0.05%). In the H-upd potential region, where H_2O_2 formation is more pronounced due to Pt blocking by H-upd adsorption, the higher loading Pt/C catalysts showed less H_2O_2 formation, which can be attributed to competing H_2O_2 reduction to water at the Pt particles.

3.4 The methanol oxidation reaction (MOR)

The activity and selectivity of the different catalysts in the MOR (10 mM CH_3OH in 0.5 M H_2SO_4, electrolyte flow rate *ca.* 10 µl s^{-1}) were studied using DEMS at room temperature, quantifying the total Faradaic current (charge) and the current efficiency (see Sect. 2) for complete methanol oxidation to CO_2. The simultaneous ORR/MOR on the respective catalysts was investigated by RDE measurements at elevated temperatures (60 °C).

3.4.1 MOR activity and selectivity

3.4.1.1 Commercial Pt/C catalysts Potentiodynamic DEMS measurements of the MOR over the commercial Pt/C catalysts (Pt loading 20 and 40 wt.%, respectively), in 10 mM methanol containing solution are shown in Fig. 7 (Faradaic (a) and mass spectrometric $m/z = 44$ (b) currents). They largely reproduce previously reported results, with a dominant oxidation peak (CO_2 formation peak) around 0.75 V in the positive-going scan, a decay at more positive potential due to PtO formation at the electrode surface, which inhibits the MOR, a strong increase in oxidation current in the negative-going scan after reduction of the Pt oxide, and finally the decay of the oxidation current upon due to CO_{ad} blocking of the catalyst surface [51 and references therein].

In the mass spectrometric measurements, methylformate formation (as indicator for formic acid production) is not

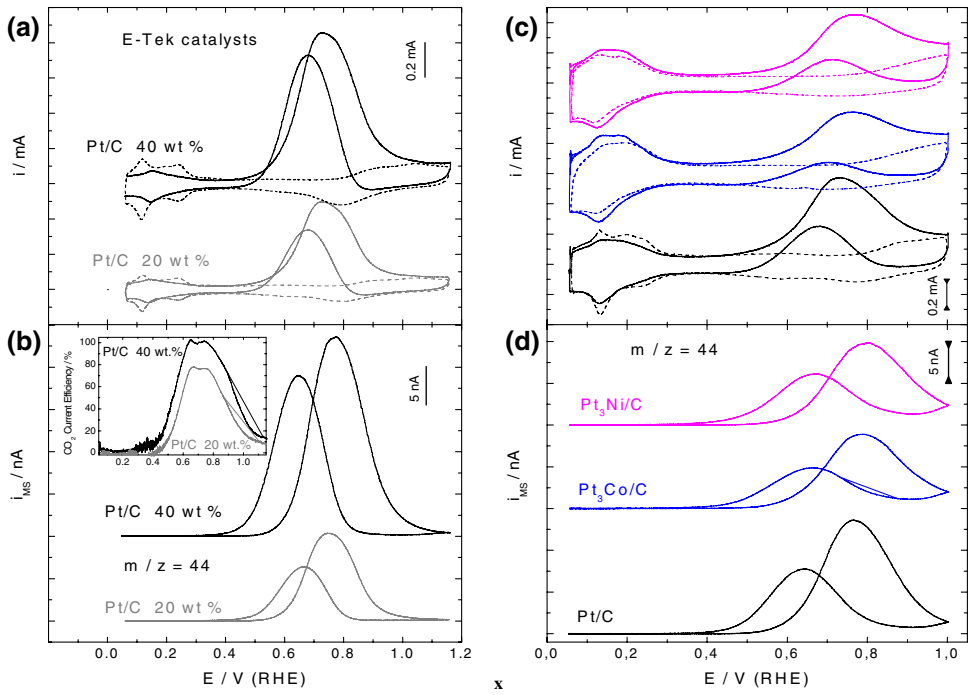

Fig. 7 Methanol oxidation on the Pt/C (20 and 40 wt.%; E-Tek) and on the synthesized Pt/C and Pt_3Me/C (Me = Ni and Co, 40 wt.%) catalysts measured in the DEMS configuration: Faradaic (**a**, **c**) and mass spectrometric (*m/z* = 44) (**b**, **d**) currents. *Inset* Fig. 7b: CO_2 current efficiency (%) determined in the positive-going scan catalyst loading 28 and 56 μg cm^{-2} for the 20 and 40 wt.%, respectively, electrolyte (0.5 M H_2SO_4 + 0.01 M CH_3OH) flow rate 10 μl s^{-1}, potential scan rate 10 mV s^{-1}, room temperature. *Dotted lines* corresponding base CVs

detectable at the low-methanol concentration used (10 mM) [52], due to both the lower amounts of formic acid produced and the low-methanol bulk concentration. Nevertheless, by converting the CO_2 formation charge (six electron oxidation of methanol to CO_2) to the corresponding partial Faradaic charge, and using the calibration constant determined for CO_{ad} stripping on Pt/C catalysts [36] (Fig. 3a, b), current efficiencies for CO_2 formation can be calculated. This way we determine CO_2 current efficiencies of *ca.* 62 and 83% over a complete potential cycle for the 20 and 40 wt.% Pt loading catalysts, respectively. In addition, the potential dependence of the CO_2 current efficiencies are included as inset in Fig. 7b. Obviously, the CO_2 current efficiency is high in the range of the peak maximum and decreases for higher potentials; apparently under those conditions incomplete methanol oxidation prevails. (At lower potentials, such kind of evaluation is complicated because of the contribution from oxidation of adsorbed species which were formed before in the scan at more cathodic potentials.) Both results clearly indicate a significant contribution of incomplete methanol oxidation to formic acid and/or formaldehyde under these conditions [51, 52]. Notably, the current efficiency for CO_2 formation is significantly higher at higher Pt loading, confirming a previously proposed concept of an increased probability for re-adsorption/further oxidation of incomplete MOR products for higher catalyst loadings or thicker catalyst layers (for detailed discussion see [34]). Based on the about double total MOR activity (Faradaic current) of the higher loading catalyst compared to that of the 20 wt.% catalyst we would not expect pronounced loading effects on the methanol tolerance.

3.4.1.2 Synthesized catalysts Figure 7c and d show the simultaneous CVs (c) and MSCVs (d) for methanol oxidation on the synthesized carbon-supported Pt (40 wt.%) and Pt_3Me (Me = Ni, Co) catalysts in 10 mM methanol/0.5 M H_2SO_4. The potentiodynamic scans on Pt/C exhibit the typical shape for Pt/C catalyst as described above. Despite the much higher surface area compared to the commercial Pt/C (40 wt.% E-Tek) catalyst, the mass spectrometric current/charge of the complete oxidation of methanol to CO_2 are lower than for the 40 wt.% commercial catalyst. The lower activity of the small particle Pt/C catalyst agrees well with previous findings of an optimum particle size for methanol oxidation, which can be explained by the higher tendency for Pt surface oxidation of smaller particles, on the one hand, and the decreasing active surface area of larger particles on the other hand [20, 22, 53, 54]. Interestingly, based on potentiodynamic and potentiostatic measurements, Tang et al. reported an optimum MOR activity for 3.8 nm Pt particles [22]. Methanol oxidation on the Pt_3Me/C (Me = Ni, Co) catalysts, results in a significantly lower MOR activity (by a factor of about 1.5) compared to the synthesized Pt/C catalyst (Fig. 7c, d), where the latter is again less active than the commercial Pt/C catalysts (by a factor of about 1.5 for similar Pt loading). Neither Ni nor Co exert a promoting effect on the onset potential for methanol oxidation, most likely since there is no measurable alloy formation, and the maximum MOR

currents are significantly lower than on the Pt/C catalyst. Considering the about equal ORR activity of the bimetallic catalysts, this indicates an improved methanol tolerance of the new bimetallic Pt_3Me/C catalysts compared to the synthesized Pt/C catalyst and, even more pronounced, compared to the commercial 40 wt.% Pt/C catalyst, in agreement with previously reported data [55–57].

In order to evaluate the CO_2 efficiency (MOR selectivity) under steady-state conditions, potentiostatic methanol oxidation experiments were performed. Faradaic (Fig. 8 a.*x*) and mass spectrometric currents transients (Fig. 8b.*x*), following the formation of CO_2 (*m/z* = 44) after a potential step from 0.06 to 0.6 V and then stepwise to 0.7 and 0.8 V (300 s per potential) on the commercial Pt/C 40 wt.% catalyst and on the synthesized carbon-supported Pt (40 wt.%) and Pt_3Me (Me = Ni, Co) catalysts, are shown in the Fig. 8. As described before, the CO_2 current efficiencies (Fig. 8c.*x*) were calculated by converting the CO_2 formation current into the corresponding partial Faradaic current and dividing this by the overall Faradaic current at the selected potential.

The shape of the methanol oxidation transients exhibits an initial spike in the Faradaic current for all catalysts after the potential step from 0.06 to 0.6 V. Subsequently the current decays continuously (around 30 s) until an approximately constant value is reached. In the mass spectrometric signal the spike is also present, though much less pronounced. (Note that the mass spectrometric data are smoothened by averaging, which reduces the time resolution.) Accordingly, the spike is not only due to double layer charging, but includes also contributions from an initially high-reaction rate, e.g., due to adsorbate oxidation. Going to higher potentials, the Faradaic current and CO_2 formation are increased on all catalysts. At more positive potential (0.8 V), the activity and selectivity decrease, due to increasing of the PtO formation at this potential, in good agreement with the potentiodynamic data (Fig. 7a, b).

These measurements reveal for all potentials higher steady-state activities for the Pt/C catalysts than for the bimetallic catalysts, with the steady state current on the synthesized Pt/C catalyst being smaller than that of the commercial Pt/C catalysts. For all potentials studied, the

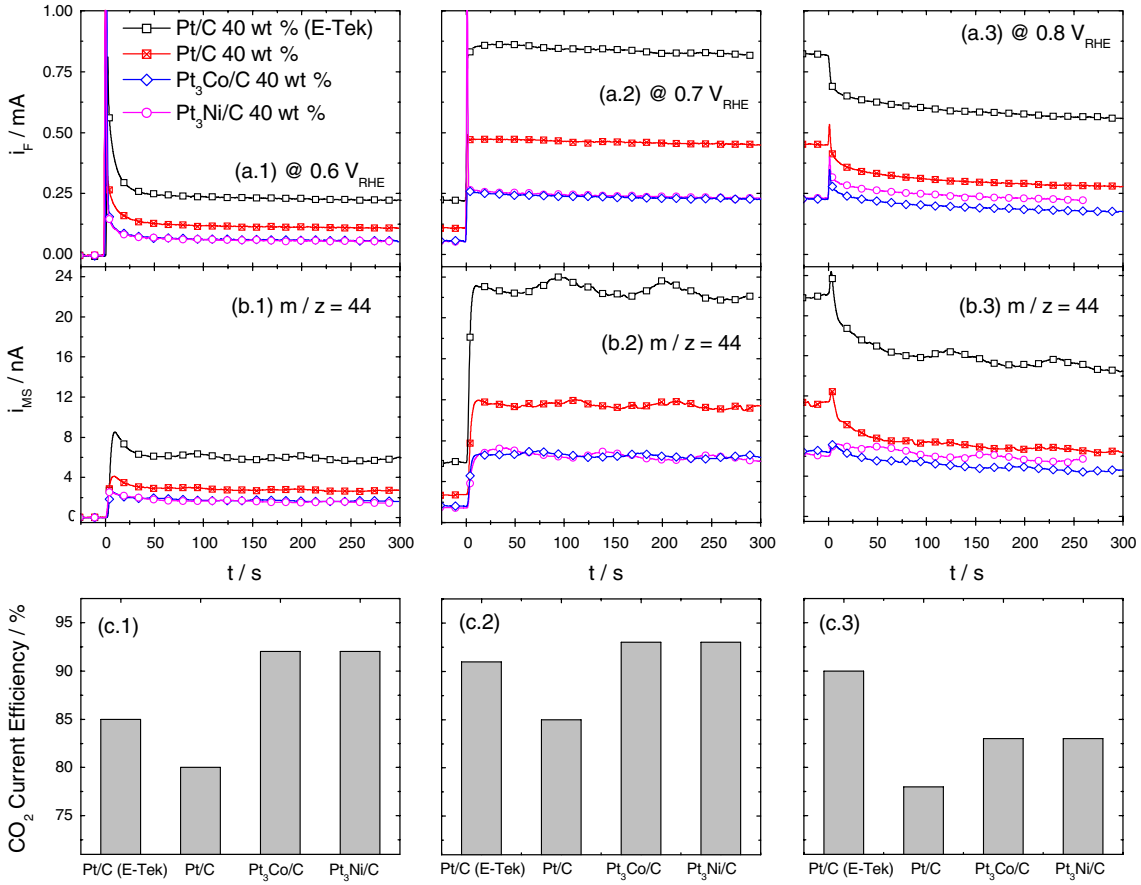

Fig. 8 Catalytic activity (**a**.*x*), mass spectrometric CO_2 currents (**b**.*x*), and selectivity for methanol oxidation to CO_2 (**c**.*x*) after a potential step from 0.06 to 0.6 V and then stepwise to 0.7 and 08 V (300 s per potential) measured on the commercial Pt/C (40 wt.%, E-Tek) and on the synthesized Pt/C and Pt_3Me/C (Me = Ni, Co) catalysts

Pt_3Me/C catalyst showed the smallest activity for the MOR. These trends reflect the features in the potentiodynamic measurements and can be rationalized in the same way. At 0.8 V, the Faradaic current on the Pt_3Ni/C is slightly higher than on the Pt_3Co/C catalyst, which may be related to further Ni dissolution.

Not only the activity, but also the selectivity for complete methanol oxidation is lower for the synthesized Pt/C catalyst than for the commercial Pt/C catalysts, independent of the potential (0.6, 0.7, and 0.8 V). This is tentatively explained by a similar particle size effect as described above. In that model, the higher tendency of the smaller particles for surface oxidation/OH formation [20] results also in lower probabilities for complete oxidation of readsorbing, partially oxidized reaction side products (formaldehyde, formic acid). On the bimetallic catalysts, the tendency for CO_2 formation is slightly higher (*ca.* 5–15%) than on the synthesized Pt/C catalyst. One may speculate that despite the absence of measurable alloy formation, the slight increase in CO_2 current efficiency could be related to Pt-Me neighborhoods.

3.4.2 Simultaneous MOR and ORR

In this section, we evaluated the influence of the methanol and the ongoing MOR (10 mM methanol in supporting electrolyte) in RDE measurements on the ORR at enhanced transport and temperatures, simulating the methanol cross-over under relevant DMFC conditions (continuous mass transport, 1,600 rpm, realistic catalysts and elevated temperatures, 60 °C). RDE measurements were performed for the MOR and ORR separately and for the ORR in methanol containing electrolyte (simultaneous MOR + ORR) [Fig. 9a: commercial Pt/C (E-Tek) catalysts; b: synthesized catalysts].

3.4.2.1 Commercial Pt/C catalysts In the presence of 10 mM methanol in deareated supporting electrolyte (0.5 M H_2SO_4), RDE measurements on these catalysts (Pt loading 20 and 40 wt.%, respectively), show a significant MOR activity (Fig. 9a), reaching higher MOR currents at higher catalyst loading, which indicates a kinetically controlled process. The MOR currents in the RDE set-up at 60 °C are significantly higher than the corresponding MOR currents in the DEMS configuration (Fig. 7a). This difference can be explained by the more vigorous mass transport of methanol to the electrode and the efficient removal of incomplete methanol oxidation products (formic acid and formaldehyde) to the bulk electrolyte [58], combined with thermal activation of the MOR [59]. When the solution of methanol (10 mM in 0.5 M H_2SO_4) is saturated with O_2, the net current in the increasing slope of the peak, at potentials lower than 0.85 V, appears to be shifted positively compared to deareated methanol solution, which actually results from the ORR induced down-shift of the base line [1–3, 52]. Since in the potential regime of the MOR peak maximum the ORR is still largely transport controlled, the combined MOR + ORR current is larger for the higher Pt loading catalyst, mainly due to the higher MOR contributions. Comparing the overpotential (η) at 0.5 mA in O_2-saturated electrolyte in the presence and absence of methanol, we find a high-negative shift of *ca.* 0.32 V, independently of the Pt catalysts loading. Hence, independent of the Pt loading both catalysts are similarly affected by the simultaneous MOR. Furthermore, for both catalysts the adsorbates produced during interaction of methanol with the catalyst do not play an important role since at more negative potentials, negative of 0.5 V, the ORR is fully transport limited and the remaining part of the Pt surface available for the ORR seems to be sufficient to reach the transport limited value, while for higher potentials, close to the transition to the kinetically controlled ORR region, the steady-state coverage of the reaction inhibiting intermediates decreases to negligible values.

3.4.2.2 Synthesized catalysts On the synthesized Pt/C catalyst, the shift in overpotential at 0.5 mA (about 0.3 V) is slightly less than on the commercial catalysts, for the Pt_3Ni/C it amounts to *ca.* 0.27 V, and for the Pt_3Co/C catalyst it is lowest with *ca.* 0.24 V. The mixed-potential E_{mix} resulting for the ORR in 10 mM methanol containing electrolyte under current reaction conditions shifts by *ca.* 75 mV to more positive values on Pt_3Co/C catalysts ($E_{mix} \approx 0.69$ V, $\eta \approx 0.26$ V, ORR onset: 0.95 V) compared to the synthesized Pt/C catalyst ($E_{mix} \approx 0.62$ V, $\eta \approx 0.33$ V, ORR onset: 0.95 V). On Pt_3Ni/C, the change of E_{mix} amounts only to *ca.* 26 mV compared to the synthesized Pt/C catalyst. In total, the synthesized Pt/C catalyst and, to a slightly greater extent, the bimetallic catalysts, are more methanol tolerant than the commercial Pt/C catalysts. The differences, however, are small, and mainly due to the higher MOR activity of the latter catalysts. Most likely, these effects are related to the smaller particle sizes of the synthesized catalysts.

In total, for all catalysts the influence of methanol on the ORR ('cross-over of methanol') was well described by an additive behavior, where the resulting current results from a simple addition of the MOR current (in O_2-free solution) and the ORR current (in methanol free solution): At lower potentials (<0.7 V), where the MOR results in a steady-state adsorbate layer on the catalyst, the ORR is mass transport limited and the remaining, uncovered catalyst area is sufficient to reach the transport limited current value. For higher potentials, where the ORR is kinetically

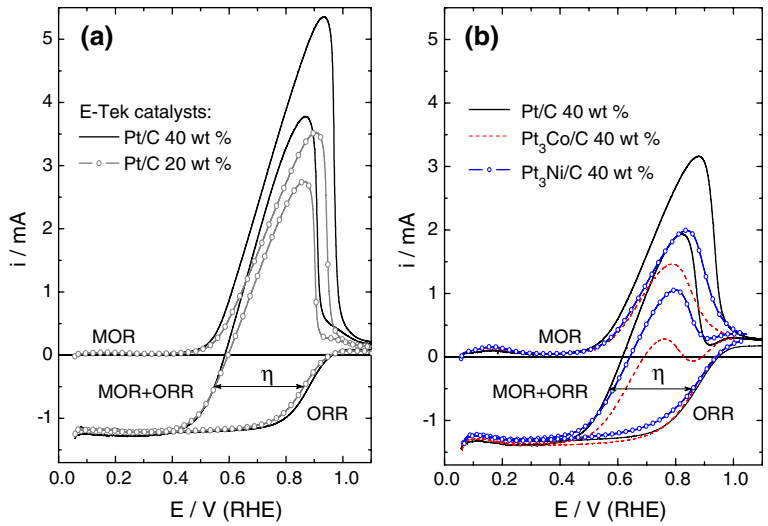

Fig. 9 O_2 reduction and methanol oxidation on **a** the commercial Pt/C (20 and 40 wt.%; E-Tek) catalysts and **b** on the synthesized Pt/C and Pt_3Me/C (Me = Ni and Co, 40 wt.%) catalysts in the RDE configuration: positive-going potential scans in deaerated (*upper set*) 0.5 M H_2SO_4 + 0.01 M CH_3OH, oxygen-saturated (*middle set*) 0.5 M H_2SO_4 + 0.01 M CH_3OH, and oxygen-saturated (*lower set*) 0.5 M H_2SO_4 electrolyte. Catalyst loading 28 and 56 μg cm^{-2} for the 20 and 40 wt.% catalyst, respectively, rotation rate 1,600 rpm, potential scan rate 10 mV s^{-1}, 60 °C

controlled, the steady-state adsorbate coverage in the MOR is negligible. The methanol induced shift in overpotential is highest for the commercial Pt/C catalyst and decreases via the synthesized Pt/C catalyst (0.3 V) to the bimetallic catalysts. The mixed potential (potential of zero current) increases in the same order. These trends reflect a measurable improvement in the methanol tolerance for the synthesized catalysts and in particular for the bimetallic catalysts, which is largely related to the lower MOR activity of the latter catalysts than changes in the ORR activity.

4 Summary

Novel carbon-supported (Black Pearl) high loading (40 wt.%) Pt/C and non-alloyed bimetallic Pt_3Me/C (Me = Ni or Co) catalysts were synthesized *via* a colloidal route and characterized with respect to particle size and chemical (surface) composition by TEM, XRD, EDX, and XPS. These measurements revealed that the alloy formation was negligible, with separate Ni(Co) particles coexisting with smaller Pt-rich particles.

Measurements of the electrochemically active surface area, performed via pre-adsorbed CO_{ad} monolayer oxidation, resulted in values which were close to those calculated from the mean particle size, except for the Pt_3Ni/C catalyst, where the active surface area would be compatible with a mean particle size of 2 nm, most likely due to a more pronounced phase separation with larger separate Ni particles. The ORR(MOR) activity, selectivity (for H_2O and CO_2 formation, respectively), and methanol tolerance of these catalysts and a commercial high-loading Pt/C catalyst were investigated by RRDE and DEMS measurements, performed under fuel cell relevant conditions, under continuous, controlled electrolyte flow at room temperature, and at elevated temperatures. At potentials relevant for cathode operation ($E > 0.7$ V), the ORR activity of the synthesized catalysts was close to that of the commercial Pt/C catalyst, and the H_2O_2 production was negligible for all catalysts (<0.05%). Potentiodynamic and potentiostatic DEMS data revealed an effective decrease of the MOR activity and a slight increase of the MOR selectivity (CO_2 current efficiency increases by *ca.* 5–15%) on the bimetallic catalysts compared to the synthesized Pt/C. Compared to the commercial Pt/C catalyst, the selectivity differences are smaller, while the activity differences become more pronounced. Finally, RDE measurements performed on all catalysts at 60 °C in methanol free and 10 mM methanol containing O_2-saturated acid solution revealed a rather low influence of methanol on the ORR ('cross-over of methanol'). The methanol induced shift in overpotential for the ORR and in the mixed potential (potential of zero current) can be described by simple addition of the MOR and the ORR currents in the respective pure electrolytes. The measurable improvement in the methanol tolerance of the synthesized catalysts and in particular for the bimetallic catalysts is largely related to their lower MOR activity rather than to changes in the ORR activity.

In total the strategy to increase the methanol tolerance by smaller particle sizes was reasonably successful, in particular for the bimetallic catalysts. Further improvements should concentrate on improved alloy formation in the latter catalysts, while maintaining the small sizes.

Acknowledgments This work was supported by the Federal Ministry of Education and Research (BMBF) within the network 'O_2 Rednet' (contract 01SF0302). L.C. is grateful for a fellowship from the Fundación Gran Mariscal Ayacucho Venezuela/DAAD. We are grateful to Dr. C. Stinner (ZSW, Ulm) and Dr. J. Cai for the XRD and XPS measurements.

References

1. Bittins-Cattaneo B, Wasmus S, Lopez de Mishima BA, Vielstich W (1993) J Appl Electrochem 23:625
2. Chu D, Gilman S (1994) J Electrochem Soc 141:1770
3. Vielstich W, Paganin VA, Lima FHB, Ticianelli EA (2001) J Electrochem Soc 148:A502–A505
4. Toda T, Igarashi H, Uchida H, Watanabe M (1999) J Electrochem Soc 146:3750
5. Paulus UA, Wokaun A, Scherer GG, Schmidt TJ, Stamenkovic V, Radmilovic V, Markovic NM, Ross PN Jr (2002) J Phys Chem B 106:4181
6. Yang H, Vogel W, Lamy C, Alonso-Vante N (2004) J Phys Chem B 108:11024
7. Li W, Zhou W, Li H, Zhou Z, Zhou B, Sun G, Xin Q (2004) Electrochim Acta 49:1045
8. Maillard F, Martin M, Gloaguen F, Leger JM (2002) Electrochim Acta 47:3431
9. Yang H, Alonso-Vante N, Leger JM, Lamy C (2004) J Phys Chem B 108:1938
10. Tributsch H, Bron M, Hilgendorf M, Schulenburg H, Dorbrandt I, Eyert V, Bogdanoff P, Fiechter S (2001) J Appl Electrochem 31:739
11. Alonso-Vante N (2003) In: Vielstich W, Gasteiger HA Lamm A (eds) Handbook of fuel cells, vol 2. Wiley, Chichester
12. Colmenares L, Jusys Z, Behm RJ (2007) J Phys Chem C 111:1273
13. Colmenares L, Jusys Z, Behm RJ (2006) Langmuir 22:10437
14. Alt H, Binder H, Lindner W, Sandstede G (1971) J Electroanal Chem 31:App 19–App 22
15. Gojkovic SL, Gupta S, Savinell RF (1999) J Electroanal Chem 462:63
16. Bron M, Radnik J, Fieber-Erdmann M, Bogdanoff P, Fiechter S (2002) J Electroanal Chem 535:113
17. Bron M, Bogdanoff P, Fiechter S, Tributsch H (2005) J Electroanal Chem 578:339
18. Wang B (2005) J Power Sources 152:1
19. Schmidt TJ, Paulus UA, Gasteiger HA, Alonso-Vante N, Behm RJ (2000) J Electrochem Soc 147:2620
20. Mayrhofer KJJ, Blizanac BB, Arenz M, Stamenkovic VR, Ross PN, Markovic NM (2005) J Phys Chem B 109:14433
21. Kabbabi A, Gloaguen F, Andolfatto F, Durand R (1994) J Electroanal Chem 373:251
22. Tang Y, Zhang L, Wang Y, Zhou Y, Gao Y, Liu C, Xing W, Lu T (2006) J Power Sources 162:124
23. Kinoshita K (1990) J Electrochem Soc 137:845
24. Peuckert M, Yoneda T, Dalla Betta RA, Boudart M (1986) J Electrochem Soc 13:944
25. Watanabe M, Sei H, Stonehart P (1989) J Electroanal Chem 261:375
26. Yano H, Inukai J, Uchida H, Watanabe M, Babu PK, Kobayashi T, Chung JH, Oldfield E, Wieckowski A (2006) Phys Chem Chem Phys 8:4932
27. Saquing CD, Cheng T-T, Aindow M, Erkey C (2004) J Phys Chem B 108:7716
28. Zhang Y, Kang D, Saquing C, Aindow M, Erkey C (2005) Ind Eng Chem Res 44:4161
29. Zhang Y, Erkey C (2005) Ind Eng Chem Res 44:5312
30. Wen F, Bönnemann H (2005) Appl Organomet Chem 19:94
31. Schmidt TJ, Gasteiger HA, Stäb GD, Urban PM, Kolb DM, Behm RJ (1998) J Electrochem Soc 145:2354
32. E-Tek Inc. product information, http://www.etek-inc.com/custom/product
33. Paulus UA, Schmidt TJ, Gasteiger HA, Behm RJ (2001) J Electrochem Soc 495:134
34. Jusys Z, Kaiser J, Behm RJ (2003) Langmuir 19:6759
35. Jusys Z, Massong H, Baltruschat H (1999) J Electrochem Soc 146:1093
36. Jusys Z, Kaiser J, Behm RJ (2001) Phys Chem Chem Phys 3:4650
37. Biegler T, Rand DAJ, Woods R (1971) J Electroanal Chem 29:269
38. Bagotzky VS, Vassilyev YB (1967) Electrochim Acta 12:1323
39. Bönnemann H, Richards RM (2001) Eur J Inorg Chem 2001(10): 2455
40. Jusys Z, Kaiser J, Behm RJ (2003) J Electroanal Chem 554–555:427
41. Tamizhmani G, Dodelte JP, Guay D (1996) J Electrochem Soc 143:18
42. Paulus UA, Schmidt TJ, Gasteiger HA (2003) In: Vielstich W, Gasteiger HA, Lamm A (eds) Handbook of fuel cells, vol 2. Wiley, Chichester
43. Higuchi E, Uchida H, Watanabe M (2005) J Electroanal Chem 583:69
44. Paulus UA, Wokaun A, Scherer GG, Schmidt TJ, Stamenkovic V, Markovic NM, Ross PN (2002) Electrochim Acta 47:3787
45. Stamenkovic VR, Fowler B, Mun BS, Wang G, Ross PN, Lucas CA, Markovic NM (2007) Science 315:493
46. Tarasevich MR, Sadkowski A, Yeager E (1983) In: Bockris JOM et al (eds) Comprehensive treatise in electrochemistry. Plenum Press, New York
47. Stamenkovic V, Schmidt TJ, Ross PN, Markovic NM (2002) J Phys Chem B 106:11970
48. Wakabayashi N, Takeichi M, Uchida H, Watanabe M (2005) J Phys Chem B 109:5836
49. Markovic N, Gasteiger HA, Ross PN (1997) J Electrochem Soc 144:1591
50. Jusys Z, Kaiser J, Behm RJ (2004) ElectrochimActa 49:1297
51. Jusys Z, Behm RJ (2001) J Phys Chem B 105:10874
52. Jusys Z, Behm RJ (2004) Electrochim Acta 49:3891
53. Takasu Y, Iwazaki T, Sugimoto W, Murakami Y (2000) Electrochem Commun 2:671
54. Bergamaski K, Pinheiro ALN, Teixeira-Neto E, Nart FC (2006) J Phys Chem B 110:19271
55. Salgado JRC, Antolini E, Gonzalez ER (2005) Appl Catal B 57:283
56. Antolini E, Salgado JRC, Gonzalez ER (2005) Appl Catal B 63:137
57. Antolini E, Salgado JRC, Gonzalez ER (2005) J Electroanal Chem 580:145
58. Gojkovic SL (2004) J Electroanal Chem 573:271
59. Wakabayashi N, Uchida H, Watanabe M (2002) Electrochem Sol Lett 5:E62